DOI: 10.37190/abb/207306

Estimation of SLP/ILP parameters inside a female breast tumor during hyperthermia with mobilized and immobilized magnetic nanoparticles

Arkadiusz Miaskowski[1], Piotr Gas[2*]

[1]Department of Electronics and Information Technology, Faculty of Electrical Engineering and Computer Science, Lublin University of Technology, Lublin, Poland

[2]Department of Electrical and Power Engineering, Faculty of Electrical Engineering, Automatics, Computer Science and Biomedical Engineering, AGH University of Krakow, Krakow, Poland

[*]Corresponding author: Piotr Gas, Department of Electrical and Power Engineering, Faculty of Electrical Engineering, Automatics, Computer Science and Biomedical Engineering, AGH University of Krakow, Krakow, Poland, e-mail address: piotr.gas@agh.edu.pl

Submitted: 28th April 2025

Accepted: 18th June 2025

Abstract

Purpose: Magnetic hyperthermia is a medical procedure for treating cancerous tumors that are medically unsuitable for resection or other treatments. It involves injecting magnetic nanoparticles (MNPs) into the cancerous tissue and applying an external alternating magnetic field (AMF) to induce heat in the target tissue. Under the influence of an AMF at radiofrequency range, eddy currents are generated, and MNPs are heated in the tumor's volume, resulting in apoptosis or necrosis. The purpose of this study is to numerically analyze the power losses generated by MNPs, such as specific loss power (SLP) and intrinsic loss power (ILP), as well as the temperature distribution during magnetic hyperthermia concerning a tumor placed in an anatomical model of the female breast. *Methods*: The AMF source was a helical induction coil with an excitation current surrounding the female breast phantom. Numerical analysis was based on the solving the Helmholtz equation for the magnetic vector potential coupled with the modified Pennes equation, using the finite element method (FEM). The numerical model under consideration included the power dissipation generated by MNPs based on the linear response theory, proposed by Rosensweig, and the Joule heating generated by eddy currents. *Results*: The authors compared the effects of MNPs concentrations on the outcome thermal profiles of irregularly shaped breast tumors. Additionally, tumor temperature profiles and SLP/ILP parameters were determined in the case of mobilized and immobilized MNPs. *Conclusions*: MNPs immobilization within the tumor microenvironment significantly diminishes magnetic losses, with a corresponding reduction of approximately 30% in specific SLP/ILP parameter values.

Key words: magnetic hyperthermia, breast cancer, linear response theory, specific loss power, intrinsic loss power, mobilized and immobilized magnetic nanoparticles

1. Introduction

Breast carcinoma remains one of the leading malignancies diagnosed among women worldwide [10]. There is a pressing demand for innovative therapies that minimize adverse side effects while effectively reducing breast cancer mortality [7],[8]. Recently, significant progress has been made in the field of loco-regional, minimally invasive hyperthermic therapies [1],[21],[24], such as radiofrequency (RF) ablation [13],[52] and microwave ablation treatments [2],[5],[23],[38]. Beyond these methods, the use of magnetic nanoparticles (MNPs) in targeted hyperthermia offers distinct advantages, including precise tumor localization and protection of adjacent healthy tissues from thermal damage [9],[11],[32],[34],[50].

Magnetic fluid hyperthermia (MFH) relies on the capability of MNPs to generate heat under exposure to an alternating magnetic field (AMF) [15],[30],[39],[43] commonly induced by planar or helical coil systems [12],[33],[45],[51]. Controlled elevation of the local temperature within the tumor microenvironment to the range of 40–45°C initiates cellular mechanisms leading to necrosis or apoptosis of malignant cells [17],[47]. Over the past decade, MFH has garnered substantial interest not only as a stand-alone treatment but also in synergistic approaches combining chemotherapy or radiotherapy [3],[4],[34],[46].

The optimization and standardization of MFH therapies are critically dependent on advanced modeling techniques and rigorous validation protocols [35]. Effective treatment is predicated on maximizing cytotoxic effects while minimizing collateral tissue damage, thus requiring precise heat characterization of MNPs and comprehensive treatment planning. However, ethical concerns, high costs of clinical trials, and infrastructural limitations have slowed the widespread adoption of exist in vivo studies, consequently hindering deeper clinical understanding. Furthermore, strict safety regulations pertaining to eddy current induction and magnetic field exposure necessitate careful adherence to accepted thresholds such as the Atkinson-Brezovich ($H \times f < 4.85 \times 10^8$ A/m/s) and Herz-Dutz ($H \times f < 5 \times 10^9$ A/m/s) safety exposure limits [37],[40]. Consequently, numerical simulations based on realistic anatomical models have emerged as powerful tools for efficacy evaluation and risk assessment prior to clinical translation.

In the similar studies, three-dimensional (3D) modeling techniques were employed to investigate the impact of MNP concentration, composite geometry, and hyperthermic treatment parameters on thermal profiles in breast cancer therapy [28],[31],[32],[39]. Nevertheless, earlier models often simplified breast anatomy into basic geometries such as semi-ellipsoids or semi-spheres [26],[38], thus failing to replicate the complexity of natural tissue heterogeneity. To overcome these limitations, the present study focuses on developing a highly realistic numerical breast phantom derived from magnetic resonance imaging (MRI) data [6], offering enhanced anatomical accuracy. Additionally, the existing literature lacks comprehensive numerical models that account for both 3D temperature distribution arising from eddy currents and single-domain magnetic power losses within anatomically correct breast structures. To bridge this gap, the current investigation incorporates calorimetric measurements performed on ferrofluids using the magneTherm™ system [16],[29], ensuring precise calibration of heat generation terms. Specific loss power (SLP) and intrinsic loss power (ILP) values validated through calorimetry are subsequently used to simulate MFH-based breast cancer treatments with enhanced fidelity.

It is important to note that the SLP values reported in standard laboratory settings [41],[20] may not accurately reflect the *in vivo* environment, where factors such as blood perfusion, tissue heterogeneity, and dynamic MNP-tissue interactions significantly influence thermal behavior. Therefore, in this work, experimentally obtained SLP/ILP values were adapted to realistic anatomical models for better predicting clinical outcomes.

Building on authors' previous developments, which presented mathematical models of single-domain magnetic losses and eddy current heating, we integrated these into a modified Pennes bioheat equation to estimate the spatiotemporal evolution of temperature. This paper further describes the anatomically accurate breast phantom developed for simulations, outlines its physical parameters, and presents detailed analyses of spatially resolved volumetric power SLP and ILP losses under varying MNP concentrations. Moreover, the distinct behaviors of mobilized and immobilized MNPs within the tumor microenvironment were investigated, shedding light on their respective contributions to localized heating efficiency. By incorporating such comprehensive modeling strategies, this study aims to contribute to the refinement of MFH protocols and to pave the way for more effective, safe, and personalized breast cancer hyperthermia treatments.

2. Basic equations governing the model

The computational simulations were conducted using an MRI-derived 3D breast model, featuring an irregularly shaped tumor, as previously detailed in the authors' previous studies [14],[31]. The model represents the 35-year-old female breast classified in the 3rd class of breast composition category C (heterogeneously dense, HD), comprising 51–75% glandular tissue alongside major anatomical components such as breast fat, subcutaneous fat, muscle, skin, and a realistic breast tumor structure, as illustrated in Fig. 1. The model have used an irregularly shaped tumor with the total mass of 3.043 g and total volume of 2.791 cm^3 [14], as shown in Fig. 2.

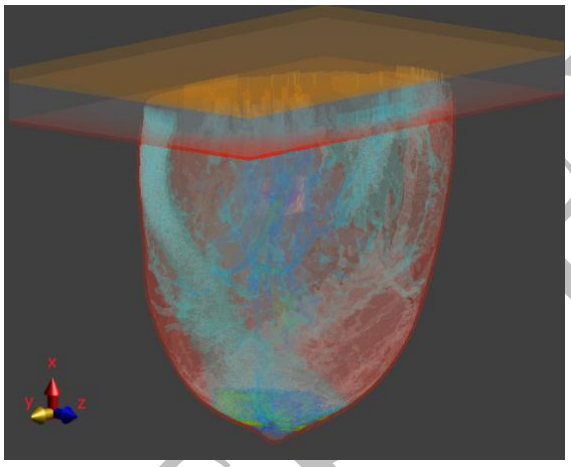

Fig. 1. MRI-derived model of female breast phantom including main breast tissues

The physical properties assigned to the various breast tissues were sourced from the Information Technologies in Society (IT'IS) database [18] and are listed in Table 1. Notably, muscle breast tissue parameters were set for the tumor. An RF coil with a radius R_{coil} = 10 cm, consisting of 10 turns, was employed, with single coil winding current of I_{coil} = 100 A and an excitation frequency f = 150 kHz positioned around the breast as shown in Fig. 2. Additionally, the coil windings were modeled as being composed of copper, characterized by an electrical conductivity of σ = 59.98 MS/m and a mass density of ρ = 8700 kg/m^3 [12], thus approximating the behavior of a perfect electric conductor (PEC) material.

Table 1. Electro-thermal parameters for 150 kHz frequency employed in the analyzed model [18] (σ – electrical conductivity, ρ – mass density, C – specific heat capacity, κ – thermal conductivity, p_{met} – metabolic heat generation, ω_b – blood perfusion rate)

Tissues	σ (S/m)	ρ (kg/m^3)	C (J/kg/K)	κ (W/m/K)	p_{met} (W/m^3)	ω_b (1/s)
skin	0.170	1109.0	3390.5	0.372	1826.52	0.001963
muscle	0.355	1090.4	3421.2	0.495	988.01	0.000674
breast gland	0.541	1040.5	2960.0	0.335	2417.08	0.002606
fat	0.057	911.0	2348.3	0.211	455.50	0.000502
breast fat	0.022	911.0	2348.3	0.209	663.03	0.000715
blood	0.660	1050.0	3617.0	0.520	0.0	0.175350
tumor	0.355	1090.4	3421.2	0.495	988.01	Eq. (21)

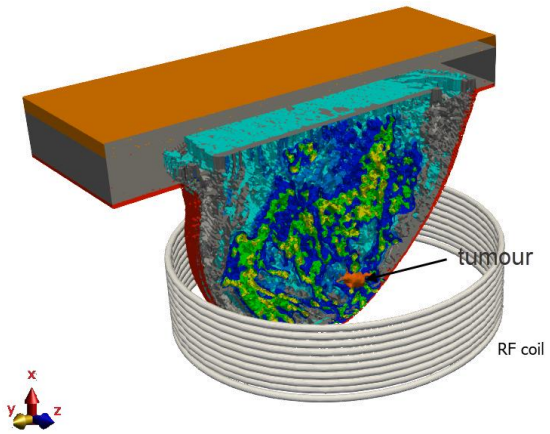

Fig. 2. Model of the 3D female breast phantom including naturalistic tumor and RF coil

2.1. Single-Domain Magnetic Power Losses Model

Based on linear response theory (LRT) [43], the heat dissipation within an individual magnetic nanoparticle (MNP) can be described by the following relation:

$$p_{\text{nano}} = \pi\mu_0 \chi'' f H^2 = \frac{1}{2}\pi\mu_0 \chi'' f H_{\max}^2 \left(\frac{\text{W}}{\text{m}^3}\right) \tag{1}$$

where $\mu_0 = 4\pi \cdot 10^{-7}$ H/m represents the permeability of free space, and χ'' means out-of-phase component of the complex magnetic susceptibility ($\chi = \chi' + j\chi''$), associated with a single MNP, defined as [25]:

$$\chi'' = \frac{\mu_0 m^2}{3k_B T} \frac{(2\pi f \tau)^2}{1+(2\pi f \tau)^2} \tag{2}$$

where k_B denotes the Boltzmann constant, $m = M_s V_M$ is the magnetic moment, M_s is the saturation magnetization, V_M is the magnetic core volume, and τ corresponds to the effective Néel-Brown relaxation time.

The specific loss power (SLP) and the intrinsic loss power (ILP) can be determined according to the following formulations [25],[41]:

$$\text{SLP} = \frac{p_{\text{nano}}}{\rho} = \frac{1}{2}\frac{\mu_0^2 M_s^2 V_M}{3k_B T \tau \rho} H_{\max}^2 \frac{(2\pi f \tau)^2}{1+(2\pi f \tau)^2} \left(\frac{\text{W}}{\text{kg}}\right) \tag{3}$$

$$\text{ILP} = \frac{\text{SLP}}{f H_{\max}^2} \left(\frac{\text{H m}^2}{\text{kg}}\right) \tag{4}$$

The characteristic Néel (τ_N) and Brownian (τ_B) relaxation times, as functions of the AMF amplitude $H_{\max}$, are given by [25]:

$$\tau_N(H_{max}) = \left(f_0(1-h^2)\left\{(1+h)\exp\left[\left(\frac{-KV_M}{k_B T}\right)(1+h)^2\right] + (1-h)\exp\left[\left(\frac{-KV_M}{k_B T}\right)(1-h)^2\right]\right\}\right)^{0.5} \quad (5)$$

$$\tau_B(H_{max}) = \tau_B\left(1+0.07\left(\frac{\mu_0\mu_r H_{max}}{k_B T}\right)\right)^{-0.5} \quad (6)$$

where $\tau_B = (3\eta V_H)/(k_B T)$ and η represents the magnetic fluid viscosity [48]. Furthermore, $h = H_{max}/H_k$ and $H_k = 2K/(\mu_0 M_s)$ defines the anisotropy field, with anisotropy constant K and $f_0 = 10^9$ s^{-1} denoting the attempt frequency.

Moreover, for spherical nanoparticles, V_M and V_H correspond respectively to the MNP magnetic core volume and the total hydrodynamic volume containing magnetic core of diameter d and coating of thickness δ, as described in [15],[41]:

$$V_M = \frac{\pi}{6}d^3 \quad , \quad V_H = \frac{\pi}{6}(d+2\delta)^3 \quad (7)$$

The coexistence of the two relaxation mechanisms results in an effective relaxation time:

$$\tau(H_{max})^{-1} = \tau_N(H_{max})^{-1} + \tau_B(H_{max})^{-1} \quad (8)$$

It is important to note that the presented model incorporates several simplifying assumptions: all MNPs are considered perfectly spherical, aggregation or chain formation, and inter-MNPs interactions are neglected. Additionally, a uniform distribution of hydrodynamic particle sizes is presumed. Under conditions of low MNPs concentration not exceed the maximum value of ϕ = 5 mg/mL, dipole-dipole interactions between nanoparticles can be considered negligible at room temperature. Therefore, in the present study, MNPs were treated as magnetically isolated entities. The physical parameters of magnetite MNPs embedded within tumor tissue are listed in Table 2.

Table 2. MNP properties employed in single-domain magnetic power losses [15], [30],[43] (M_s–saturation magnetization, K–anisotropy constant, k_B–Boltzmann constant, T–temperature, η–magnetic fluid viscosity ϕ–concentration of MNPs, d–diameter of magnetic core, δ–thicknessMNP coating)

Material	M_s (kA/m)	K (kJ/m^3)	k_B (J/K)	T (°C)	η (kg/m/s)	ϕ (mg/mL)	d (nm)	δ (nm)
magnetite (Fe_3O_4)	92.0	30	1.38×10^{-23}	25	8.94×10^{-23}	5.0	15	2.0

2.2.Eddy Current Effect Model

When biological tissues are subjected to a RF ranged AMF, eddy currents are induced due to the finite electrical conductivity of the tissues, ultimately causing heat generation.

The distribution of the AMF can be analyzed using the magneto-quasistatic approximation applicable at low frequencies [27]:

$$\mathbf{J}_e = \nabla \times \mathbf{H} = \nabla \times \mu^{-1}\mathbf{B} = \nabla \times \mu^{-1}(\nabla \times \mathbf{A}) \quad (9)$$

where $\mathbf{J}_e$ represents the excitation current density (A/m^2), $\mathbf{H}$ is the vector of magnetic field intensity (A/m), $\mathbf{B}$ denotes the vector of magnetic induction (T), $\mathbf{A}$ is the magnetic vector potential (A·m), and $\mu = \mu_0\mu_r$ is the magnetic permeability of the medium.

Utilizing the vector identity $\nabla \times (\nabla \times \mathbf{A}) = \nabla(\nabla\cdot\mathbf{A}) - \nabla^2\mathbf{A}$ and applying the Coulomb gauge condition ($\nabla\cdot\mathbf{A} = 0$), Eq. (9) simplifies to:

$$\mathbf{J}_e = -\nabla\cdot\left(\mu^{-1}\nabla\mathbf{A}\right) = -\mu^{-1}\nabla^2\mathbf{A} \tag{10}$$

Furthermore, starting from Faraday's law and employing the fundamental relation between $\mathbf{B}$ and $\mathbf{A}$ vectors [15], namely:

$$\nabla\times\mathbf{E} = -\frac{\partial\mathbf{B}}{\partial t} \tag{11}$$

$$\mathbf{B} = \nabla\times\mathbf{A} \tag{12}$$

the equivalent equations can be derived as:

$$\nabla\times\mathbf{E} = -\frac{\partial}{\partial t}\left(\nabla\times\mathbf{A}\right) = -\nabla\times\frac{\partial\mathbf{A}}{\partial t} \tag{13}$$

$$\nabla\times\left(\mathbf{E} + \frac{\partial\mathbf{A}}{\partial t}\right) = 0 \tag{14}$$

where $\mathbf{E}$ (V/m) is a vector of electric field strength. After introducing the electric scalar potential φ (V), we get:

$$\mathbf{E} = -\nabla\varphi - \frac{\partial\mathbf{A}}{\partial t} \tag{16}$$

In order to account for the volumetric power density (p_{eddy}) arising from the eddy current (J_{eddy}) effect, a magneto-quasistatic model is utilized. Incorporating the potentials φ and $\mathbf{A}$, the governing equation can formulate as:

$$\mathbf{J}_{\text{eddy}} = \sigma\mathbf{E} = -\sigma\nabla\varphi - \sigma\frac{\partial\mathbf{A}}{\partial t} \tag{17}$$

where σ is the electrical conductivity (S/m), and $\omega = 2\pi f$ (rad/s) denotes the angular frequency. Consequently, the volumetric heat generation due to eddy currents can be expressed as:

$$p_{\text{eddy}} = \sigma^{-1}J_{\text{eddy}}^2 \tag{18}$$

A detailed discussion of eddy currents, also referred to as Foucault currents, is crucial because their presence can cause unintended heating of non-targeted healthy tissues when exposed to an AMF. Therefore, their influence must be carefully addressed during the applicator design phase and throughout treatment planning.

Additionally, the vector of excitation current density generated by a multi-turn helical coil with alternating current is modeled as [15]:

$$\mathbf{J}_e = \frac{I}{S}\mathbf{e}_{\text{coil}} = \frac{NI_{\text{coil}}}{S}\mathbf{e}_{\text{coil}} \tag{19}$$

where I denotes the total current passing through the coil, N is the number of turns, I_{coil} is the current in a single loop, S represents the cross-sectional area of the coil, and $\mathbf{e}_{coil}$ is the unit vector tangent to the excitation coil.

2.3.Pennes Equation

A numerical framework for analyzing heat transfer within human tissues was originally introduced by Pennes [36]. In this formulation, blood perfusion is treated as spatially uniform across the tissue, with the assumption that all heat departing from the arterial blood is completely absorbed by the surrounding tissue, neglecting any venous rewarming effects. What is more, the Pennes model considers only a perfusion source term, presuming that the arterial blood temperature matches the body's core temperature.

Consequently, the thermal distribution in the breast model was evaluated using a modified bioheat transfer equation [19],[36]:

$$\rho C \frac{\partial T}{\partial t} = \nabla \cdot (\kappa \nabla T) + \rho_b \, C_b \, \omega_b (T)(T_b - T) + p_{met} + p_{nano} + p_{eddy} \tag{20}$$

where ρ is the tissue density (kg/m³), C is the tissue specific heat capacity (J/kg/K), ρ_b is the blood density (kg/m³), C_b is the blood specific heat capacity (J/kg/K), κ represents the thermal conductivity of tissue (W/m/K), $\omega(T)$ is the temperature-dependent blood perfusion rate (1/s), T_b is the arterial blood temperature (K), T is the local tissue temperature (K), p_{met} (W/m³) denotes metabolic heat generation, $p_{nano} = \rho SLP$ (W/m³) represents external heat generation due to magnetic nanoparticles (MNPs), and p_{eddy} (W/m³) accounts for the heat contribution from eddy currents.

To incorporate temperature-dependent physiological regulation effects [49], the blood perfusion rate in healthy breast tissues was considered as constant $\omega_b(T) = \rho\omega$ = const, whereas the perfusion within tumor tissue was modeled as a nonlinear function described by [28]:

$$\omega_{tumor}(T) = 0.4 + 0.4 \exp\left[-\frac{(T-37)^4}{880} \right] \left(\frac{\mathrm{m}^3}{\mathrm{kg\,s}} \right) \tag{21}$$

For simulating heat exchange between the skin surface and the external environment, a mixed convection-radiation boundary condition was applied [22]:

$$\kappa_{skin} \frac{\partial T}{\partial n} = h_t (T_{ext} - T) \tag{22}$$

where $h_t = 4\sigma_{SB} T^3_{ext}$ [28] is the combined heat transfer coefficient, κ_{skin} is the thermal conductivity of the skin tissue, $\sigma_{SB} = 5.67 \cdot 10^{-8}$ W/m²/K⁴ denotes the Stefan-Boltzmann constant, and $T_{ext} = 25$°C is the ambient temperature. The initial tissue temperature was assumed as $T_0 = 37$°C, while the arterial blood temperature was maintained at a constant $T_b = 37$°C. All finite element method (FEM) simulations were performed using the commercially available Sim4Life software [44].

3. Simulation results and disscusion

The mathematical model described in the previous section was used to investigate the temperature distribution during magnetic hyperthermia treatment.

The alternating current (AC) passing through the 10-turn coil (I_{coil} = 100 A, f = 150 kHz) created an alternating electric field, which induced an AMF inside the RF coil as depicted in Fig. 3a.

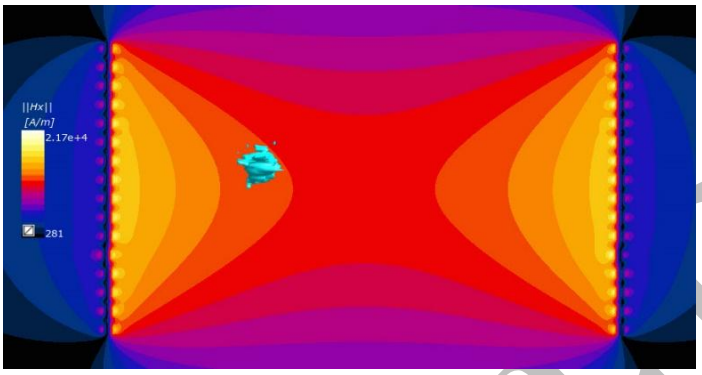

(a)

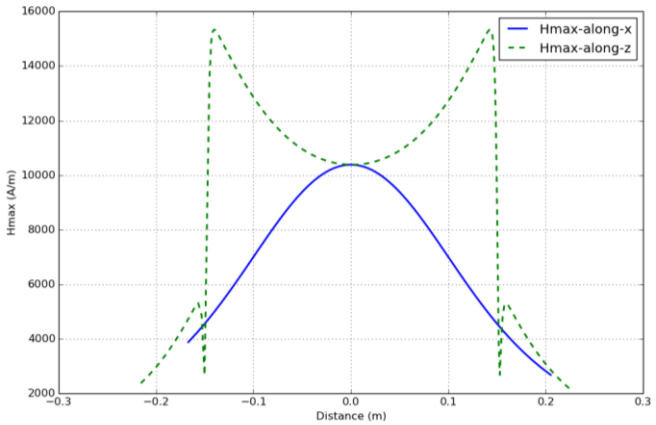

(b)

Fig. 3. Magnetic field strength distributions inside the 10-turn RF coil: a) spatial distribution on the *xy*-plane, and b) H_{max} curves along the *x*-axis (blue) and *z*-axis (green)

In the middle of the excitation coil, magnetic field strength had value of H_{max} = 10.3 kA/m (see Fig. 3b), and in the tumor location it has value of about 12 kA/m. The maximum exposure limit in the breast tissues is on the level of $H_{max} \times f = 16 \cdot 10^3 \times 1.5 \cdot 10^5 = 24 \cdot 10^8$ A/m/s. Although it exceeds the Atkinson-Brezovich safety limit equal to $4.85 \cdot 10^8$ A/m/s, but does not exceed the safety exposure limit defined by Hertz-Dutz ($5 \cdot 10^9$ A/m/s) [3],[37]. Therefore, the MNP hyperthermia may be considered safe for healthy breast tissues.

The volumetric power density due to the eddy currents was evaluated for frequency f = 150 kHz, and their distributions, after a 25-min magnetic hyperthermia procedure, are shown in Fig. 4. It is obvious that the highest value of eddy power density occurred on the skin tissue, reaching 80 kW/m^3. That is why the data was rescaled to the maximum value (40 kW/m^3), i.e., to one of the *hot spots*, which were placed in the model excluding the skin layer to improve visualization. It is important to note that the presence of hot spots should be considered during treatment planning as they are hard to predict and they can limit the amount of energy that can be deposited in a patient's body. Moreover, one should remember that maximal electrical power losses will occur on the surface of the tumor (see Fig. 4b) as the eddy currents have to circulate

around the tumor center where they are the smallest. This sometimes can be used as an advantage because high-conductivity tumors surrounded by low-conductivity tissues will have a local eddy current flowing around the approximate center of the tumor leading to increased heating of deep-seated tumors.

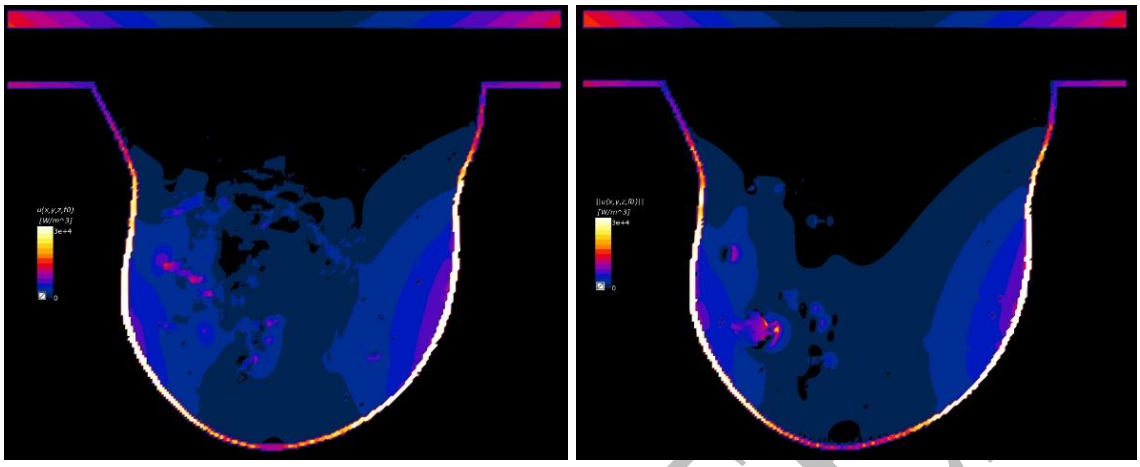

(a) (b)

Fig. 4. Eddy currents power losses in *xz*-plane in the case of female breast model: a) without tumor, and b) with tumor after the 25-min magnetic hyperthermia treatment

One can see that the tumor position has changed the power distribution pattern and the *hot spot* shifted due to the physical properties of the tumor. It corresponds to the spatial temperature distributions, presented in Fig. 5, where the temperature in breast tissues does not exceed 40°C (see Fig. 5a), and the tumor temperature reaches a higher value of 39°C (see Fig. 5b).

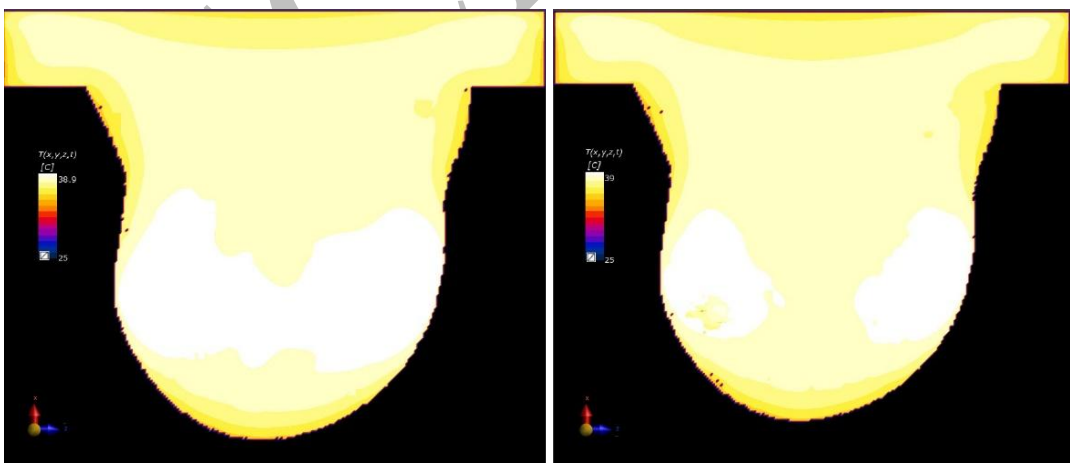

(a) (b)

Fig. 5. Temperature distributions in *xz*-plane due to eddy currents in the case of female breast model: a) without tumor, and b) with tumor after the 25-min magnetic hyperthermia treatment

To enhance the thermal effect, magnetite MNPs were injected into the tumor and their concentration was changed to control the temperature in the target tissue as shown in Fig. 6.

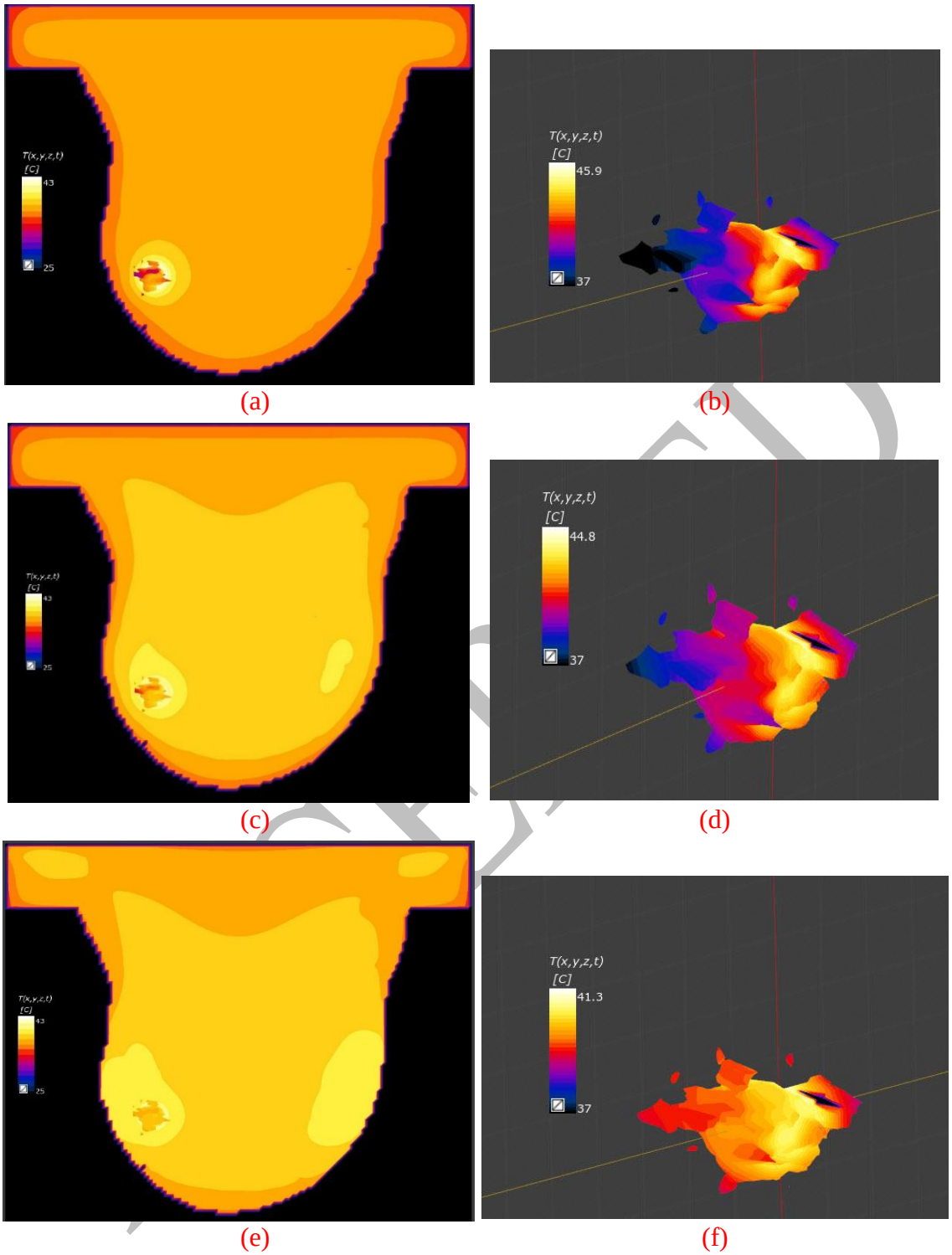

Fig. 6. Temperature distributions in *xz*-plane inside the breast model (a,c,e) and on tumor surface (b,d,e) due to MNPs concentrations in the case of relative MNPs concentrations a), b) $\phi_r = 1$, c), d) $\phi_r = 0.5$, and e), f) $\phi_r = 0.3$ with regard to maximum MNPs concentration $\phi = 5$ mg/mL after 25-min magnetic hyperthermia treatment.

In this investigation, three scenarios of MNP concentrations were considered, determined by relative MNP concentrations $\phi_r = \{1, 0.5, 0.3\}$ with regard to maximum MNP concentration $\phi = 5$mg/mL. It should be noted that the higher the ferrofluid concentration, the

higher the tumor temperature values have been observed. The maximum temperatures at the tumor surface were 45.9°C, 44.8°C, and 41.3°C, respectively. This means that even low concentrations of magnetic fluid provide adequate therapeutic temperature levels for magnetic hyperthermia treatment. To highlight the effect of MNP heating, temperature distributions were mapped in the range from 25 to 43°C.

In the next part, particular interest was paid to the comparative analysis of MNP-tissue interactions, and the heating rates of MNPs, which were determined using Néel and Brownian relaxation losses that can be inappropriate for magnetic hyperthermia treatment. For a reliable model of MNP heating, two cases were considered: 1) the mobilized MNPs free to move in the tumor, where Néel and Brownian relaxation times are included in the tumor as shown in Eq. (8); 2) the immobilized MNPs that can not move in the tumor, in which only Néel relaxation takes place and is included in Eq. (8). Time-dependent tumor temperature profiles for mobilized and immobilized MNPs in the case of different MNPs concentrations are compared in Fig. 7.

The presented characteristics show that the tumor temperature after the 25-min treatment exposure is always significantly higher in the case of mobilized than for immobilized MNPs. Moreover, the values of maximum magnetic power losses in the form of SLP/ILP parameters for the different relative MNP concentrations ϕ_r are given in Table 3. As expected, the values of these parameters decrease with decreasing ferrofluid concentration, which is reflected, in lower magnetic power losses, and as previously shown, in lower tumor temperatures. What is important, the relative difference between SLP/ILP parameters in the case of mobilized and immobilized MNPs models is about 30%.

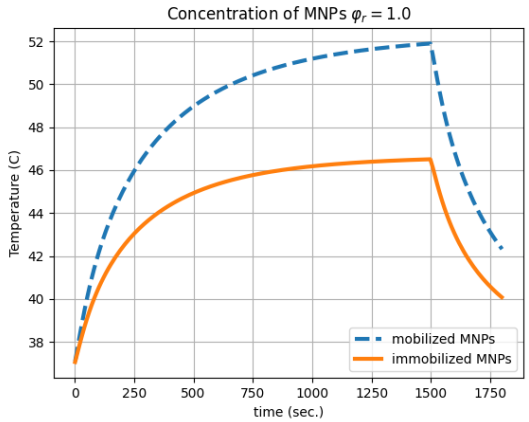

(a)

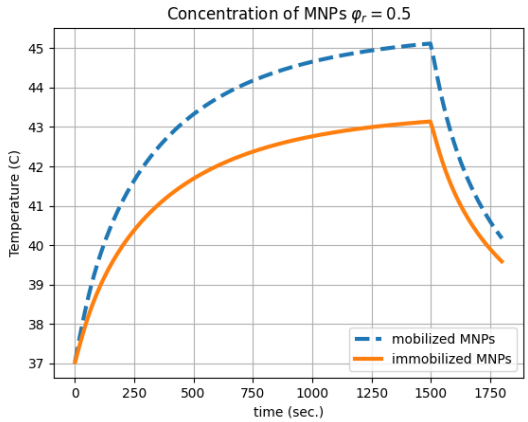

(b)

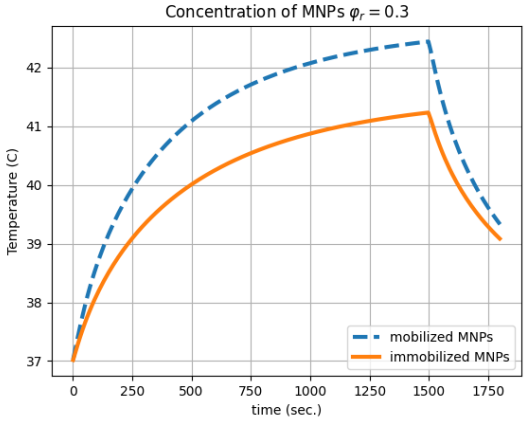

(c)

Fig. 7. Transient temperature distributions inside the tumor center in the case of mobilized and immobilized MNPs for different relative MNPs concentrations: a) ϕ_r = 1, b) ϕ_r = 0.5, and c) ϕ_r = 0.3 with regard to maximum MNPs concentration ϕ = 5 mg/mL

Table 3. Magnetic power loss parameters with regard to the relative MNP concentration inside the tumor

Relative MNPs concentrations ϕ_r (–)	**Magnetic Power Loss Parameters**				**Difference between mobilized and immobilized MNPs models**
	SLP (W/kg)	**ILP** (nH m^2/kg)	**SLP** (W/kg)	**ILP** (nH m^2/kg)	
	Mobilized MNPs		**Immobilized MNPs**		
1.0	222.85	0.010	155.91	0.007	30.0%
0.5	110.97	0.005	77.22	0.004	30.4%
0.3	66.76	0.003	46.96	0.002	29.7%

4. Conclusions

In current investigation a modified Pennes bioheat equation incorporating mixed boundary conditions was employed to evaluate the thermal profile within a realistic breast phantom. The single-domain and eddy current-induced power loss densities, treated as two main external heat sources, were implemented. The analysis revealed that, due to the complex anatomical composition of breast tissues, localized regions of elevated temperature in the form of hot spots when temperature gradients could arise to high values. These findings underscore the necessity of considering such heterogeneities in the treatment planning of magnetic hyperthermia therapies.

Performed simulation results show that the non-uniform distributions of magnetic power dissipation and temperature was observed within the tumor region. The study further highlighted the critical influence of magnetic nanoparticle (MNP) concentration on the therapeutic efficacy of magnetic hyperthermia procedure. Investigation of ferrofluid dynamics demonstrated that MNPs immobilization within the tumor microenvironment significantly diminishes magnetic losses, with a corresponding reduction of approximately 30% in specific loss power (SLP) and intrinsic loss power (ILP) parameter values. Therefore, determining the mobility status of MNPs in the magnetic fluid versus their fixation in cancerous tissue is

paramount, as MNP-tissue interactions substantially impact on hyperthermia treatment outcomes.

Summarizing, from the perspective of magnetic fluid hyperthermia (MFH) treatment planning, mitigating thermal damage to adjacent healthy tissues is essential. Special focus should be placed on the thermal gradients surrounding the tumor site. The precision of magnetic fluid-based thermal therapies is a determining factor in the success of individualized treatment protocols, and insufficient heating of tumor regions can compromise therapeutic efficacy. Consequently, the developed computational framework supports the calibration of magnetic fluid temperature monitoring under RF ranged magnetic fields exposure. Furthermore, realistic phantom-based models, such as the one proposed herein, facilitate magnetic hyperthermia procedure effectiveness evaluation before further clinical treatment.

References

[1] ACAR B., YILMAZ ABDOLSAHEB T.U.B.A., YAPAR A., *Advanced hyperthermia treatment: optimizing microwave energy focus for breast cancer therapy*, Turk J Electr Eng Comput Sci, 2024, 32(2):268–284, DOI: 10.55730/1300-0632.4068.

[2] AHAMED K.P.S., ARUNACHALAM K., *Multifrequency operation of an intracavitary monopole with sliding broadband choke for delivering hyperthermia treatment with variable coverage*, Electromagn Biol Med, 2024, 43(4):256–266, DOI: 10.1080/15368378.2024.2389068.

[3] BORGES R., SOUZA A.C.S., GENOVA L.A., MACHADO JR J., JUSTO G.Z., MARCHI J., *Biocompatible glasses applied in cancer treatment: Magnetic hyperthermia and brachytherapy*, Bioactive Glasses and Glass-Ceramics: Fundamentals and Applications, 2022, 537–579, DOI: 10.1002/9781119724193.ch22

[4] BORKOWSKA A.M., CHMIEL P., RUTKOWSKI P., TELEJKO M., SPALEK M.J., *Radiotherapy combined with locoregional hyperthermia for oligoprogression in metastatic melanoma local control*, Ther Adv Med Oncol, 2025, 17, DOI: 10.1177/17588359251316189

[5] BOSKOVIC N., RADJENOVIC B., NIKOLIC S., RADMILOVIC-RADJENOVIC M., *Effectiveness of microwave ablation using two simultaneous antennas for liver malignancy treatment*, Open Phys, 2024, 22(1), DOI: 10.1515/phys-2024-0079.

[6] ZASTROW E., DAVIS S.K., LAZEBNIK M., KELCZ F.,VAN VEEN B.D., HAGNESS S.C., Database of 3D Grid-Based Numerical Breast Phantoms for use in Computational Electromagnetics Simulations, Department of Electrical and Computer Engineering University of Wisconsin-Madison, Available at website (27 May 2025): https://uwcem.ece.wisc.edu/MRIdatabase/InstructionManual.pdf

[7] CARRIERO S., LANZA C., PELLEGRINO G., ASCENTI V., SATTIN C., PIZZI C., ANGILERI S.A., BIONDETTI P., IANNIELLO A.A., PIACENTINO F., LAVORATO R., IERARDI A.M., CARRAFIELLO G., *Ablative therapies for breast cancer: state of art*, Technol Cancer Res Treat, 2023, 22, DOI: 10.1177/15330338231157193.

[8] DEIPOLYI A.R., WARD R.C., RIAZ A., VOGL T.J., SIMMONS R.M., PIEPER C.C., BRYCE Y., *Locoregional therapies for primary and metastatic breast cancer: AJR expert panel narrative review*, Am J Roentgenol, 2024, 222(2), DOI: 2214/AJR.23.29454.

[9] FAKHRADINI S.S., MOSHARAF-DEHKORDI M., AHMADIKIA H., *Improved liver cancer hyperthermia treatment and optimized microwave antenna power with magnetic nanoparticles*, Heat and Mass Transfer, 2024, 60:1235–1250, DOI: 10.1007/s00231-024-03489-6.

[10] FUENTES J.D.B., MORGAN E., DE LUNA AGUILAR A., MAFRA A., SHAH R., GIUSTI F., VIGNAT J., ZNAOR A., MUSETTI C., YIP C.-H., VAN EYCKEN L., JEDY-AGBA E., PINEROS M., SOERJOMATARAM I., *Global stage distribution of breast cancer at diagnosis: a systematic review and meta-analysis*, JAMA Oncol, 2024, 10(1):71–78, DOI: 10.1001/jamaoncol.2023.4837.

[11] FRONYA A.A., DONCHENKO D.V., MAVRESHKO E.I., TUPITSYN I.M., GRIGORYEVA M.S., ZAVESTOVSKAYA I.N., *Study of the Dynamics of Dissolution and Laser Heating of Germanium Nanoparticles*, Bulletin of the Lebedev Physics Institute, 2024, 51(12):601–606, DOI:10.3103/S1068335624601535.

[12] GAS P., *Behavior of helical coil with water cooling channel and temperature dependent conductivity of copper winding used for MFH purpose*, IOP Conf. Ser. Earth Environ. Sci., 2019, 214(1), DOI: 10.1088/1755-1315/214/1/012124.

[13] GAS P., MIASKOWSKI A., *Influence of the radiofrequency applicators arrangement on the sizes of ablative zones inside hepatic tumor*, Arch. Electr. Eng., 2024, 73(3):557–571, DOI: 10.24425/aee.2024.150883.
[14] GAS P., MIASKOWSKI A., *Numerical estimation of SAR and temperature distributions inside differently shaped female breast tumors during radio-frequency ablation*, Materials, 2022, 16(1), DOI: 10.3390/ma16010223.
[15] GAS P., SULEMAN M., KHALIQ F., *3D computational modeling of Fe3O4@Au nanoparticles in hyperthermia treatment of skin cancer*, Nanotechnol Sci Appl, 2025, 18:173–196, DOI: 10.2147/NSA.S495377.
[16] GAS P., MIASKOWSKI A., *Specifying the ferrofluid parameters important from the viewpoint of magnetic fluid hyperthermia*, 2015 Selected Problems of Electrical Engineering and Electronics (WZEE), 2015, 1–6, DOI: 10.1109/WZEE.2015.7394040.
[17] HARMON B.V., FORSTER T.H., COLLINS R.J., Hyperthermia-induced apoptosis, Programmed Cell Death, 2024, 297–314.
[18] HASGALL P.A., DI GENNARO F., BAUMGARTNER C., NEUFELD E., LLOYD B., GOSSELIN M.C., PAYNE D., KLINGENBOCK A., KUSTER N., *IT'IS database for thermal and electromagnetic parameters of biological tissues, IT'IS Foundation*, 2022, version 4.1, DOI: 10.13099/VIP21000-04-1.
[19] HSSEINIMOTLAGH S.N., FERESHTEH M., SHAKERI A., MOKHTARI M., RASTI F., ZAREI M.A., Modeling of heat transfer to different human cancerous tissues using magnetic nanoparticles, Degres J, 2024, 9(8):89–102, DOI: 12.1789001.DEJ.2024.V9I8.24.411837.
[20] IACOB N., *Pitfalls and challenges in specific absorption rate evaluation for functionalized and coated magnetic nanoparticles used in magnetic fluid hyperthermia*, Coatings, 2025, 15(3), DOI: 10.3390/coatings15030345.
[21] IMANLOU S., VAFAI K., *Hyperthermia applications in cardiovascular and cancer therapy treatments*, Adv Heat Transf, 2024, 57:71–99, DOI: 10.1016/bs.aiht.2024.02.002.
[22] KAZEMI ALOUTI A., RAOUF I., ZAHABI S., SALIMIBANI M., *Numerical study of magnetic nanoparticles injection into a brain tumor considering the effects of injection volume and location on the termination of cancerous cells*, Biointerphases, 2024, 19(6), DOI: 10.1116/6.0003814.
[23] KIM D., KIM H., *Optimal condition confirmation of treatment conditions through analysis of intratumoral apoptotic temperature range of microwave ablation for various microwave frequencies and antenna insertion depth*, Sci Prog, 2024, 107(4), DOI: 10.1177/00368504241300855.
[24] KSHATRIYA V.V., KUMBHARE M.R., JADHAV S.V., THORAT P.J., BHAMBARGE R.G., *A review on electromedicine its various properties and emerging application in various fields*, Intell Pharm, 2024, 6:777–783, DOI: 10.1016/j.ipha.2024.05.001.
[25] MAMIYA H., *Recent advances in understanding magnetic nanoparticles in AC magnetic fields and optimal design for targeted hyperthermia*, J Nanomater, 2013, 2013, DOI: 10.1155/2013/752973.
[26] MANSOR HASSAN M., LIAS K., BUNIYAMIN N., AHMAD NARIHAN M.Z., SHEIKH NAIMULLAH B.S., MOHAMED BASRI H., ALAM S., *SAR distribution with different water bolus shapes for hyperthermia breast cancer treatment*, J Adv Res Fluid Mech Therm Sci, 2025, 128(1):32–47, DOI: 10.37934/arfmts.128.1.3247.
[27] MAXWELL J.C., *VIII. A dynamical theory of the electromagnetic field*, Philos Trans R Soc Lond, 1865, 155:459–512, DOI: 10.1098/rstl.1865.0008.

[28] MIASKOWSKI A., GAS P., *Modelling of temperature distribution in anatomically correct female breast cancer*, Prz Elektrotechniczn, 2022, 99(2):218–221, DOI: 10.15199/48.2023.02.42.
[29] MIASKOWSKI A., SAWICKI B., SUBRAMANIAN M., *Single-domain nanoparticle magnetic power losses calibrated with calorimetric measurements*, Bull Pol Acad Sci Tech Sci, 2018, 66(4):509–516, DOI: 10.24425/123928.
[30] MIASKOWSKI A., SUBRAMANIAN M., *Numerical model for magnetic fluid hyperthermia in a realistic breast phantom: calorimetric calibration and treatment planning*, Int J Mol Sci, 2019, 20(18), DOI: 10.3390/ijms20184644.
[31] MICHALOWSKA-SAMONEK J., MIASKOWSKI A., WAC-WLODARCZYK A., *Numerical analysis of high frequency electromagnetic field distribution and specific absorption rate in realistic breast models*, Prz Elektrotechniczn, 2012, 88(12b), pp. 97–99.
[32] NAIN S., KUMAR N., AVTI P.K., *Effect of arterial blood flow on magnetic nanoparticle thermo-therapy applied on a realistic breast tumor model*, Int J Numer Methods Biomed Eng, 2025. 41(4), DOI: 10.1002/cnm.70039.
[33] NOEREN J., GOTZ T.D., ELBRACHT L., PARSPOUR N., *Quality factor comparison of pipe coils in wireless charging applications*, IEEE Wireless Power Technol. Conf. Expo (WPTCE), 2024, 816–820, DOI: 10.1109/WPTCE59894.2024.10557435.
[34] OVERGAARD J., HULSHOF M.C., DAHL O., ARCANGELI G., *Hyperthermia as an adjuvant to radiation therapy in the treatment of locally advanced breast carcinoma*, Radiother Oncol, 2024, 196, DOI: 10.1016/j.radonc.2024.110313.
[35] PARUCH M., *Hyperthermia process control induced by the electric field in order to cancer destroying*, Acta Bioeng Biomech, 2014, 16(4): 123–130, DOI: 10.5277/ABB-00075-2014-02.
[36] PENNES H.H., *Analysis of tissue and arterial blood temperatures in the resting human forearm*, J Appl Physiol, 1998, 85(1):5–34, DOI: 10.1152/jappl.1998.85.1.5.
[37] PILPILIDIS K., TSANIDIS G., ROUNI M.A., MARKAKIS J., SAMARAS T., *Revisiting the safety limit in magnetic nanoparticle hyperthermia: insights from eddy current induced heating*, Phys Med Biol, 2025, 70(3), DOI: 10.1088/1361-6560/adaad0.
[38] PINTO GARCIA E., CEPEDA RUBIO M.F.J., GUERRERO LOPEZ G.D., SEGURA FELIX K., HERNANDEZ JAQUEZ J.I., FLORES GARCIA F., *Impact of breast tissue heterogeneity on microwave ablation performance: insights from computational modeling*, Curr Cancer Ther Rev, 2025, 21(4):57–585, DOI: 10.2174/0115733947299809240804192844.
[39] RAHPEIMA R., LIN C.A., *Numerical study of magnetic hyperthermia ablation of breast tumor on an anatomically realistic breast phantom*, PLoS One, 2022, 17(9), DOI: 10.1371/journal.pone.0274801.
[40] RAOUF I., GAS P., KIM H.S., *Advances in finite element analysis for cancer therapy focusing on magnetic nanoparticle hyperthermia*, Multiscale Sci Eng, 2024, 6(2–3):113–123, DOI: 10.1007/s42493-024-00116-8.
[41] RAOUF I., GAS P., KIM H.S., *Numerical investigation of ferrofluid preparation during in-vitro culture of cancer therapy for magnetic nanoparticle hyperthermia*, Sensors, 2021, 21(16), DOI: 10.3390/s21165545.
[42] RIAZ S., ALI S., SUMMER M., AKHTAR U., NOOR S., HAQQI R., FAROOQ M.A., SARDAR I., *Multifunctional magnetic nanoparticles for targeted drug delivery against cancer: a review of mechanisms, applications, consequences, limitations, and tailoring strategies*, Ann Biomed Eng, 2025, DOI: 10.1007/s10439-025-03712-3.

[43] ROSENSWEIG R.E., *Heating magnetic fluid with alternating magnetic field*, J Magn Magn Mater, 2002, 252:370–374, DOI: 10.1016/S0304-8853(02)00706-0.
[44] SIM4LIFE, Manual, Version 6.2, Zurich MedTech AG, Zurich, Switzerland, 2021. https://sim4life.swiss/
[45] SUBRAMANIAN M., MIASKOWSKI A., PEARCE G., DOBSON J., *A coil system for real-time magnetic fluid hyperthermia microscopy studies*, Int J Hyperthermia, 2016, 32(2):112–120, DOI: 10.3109/02656736.2015.1104732.
[46] SUN R., CHEN H., WANG M., YOSHITOMI T., TAKEGUCHI M., KAWAZOE N., YANG Y., CHEN G., *Smart composite scaffold to synchronize magnetic hyperthermia and chemotherapy for efficient breast cancer therapy*, Biomaterials, 2024, 307, DOI: 10.1016/j.biomaterials.2024.122511.
[47] SZWED M., MARCZAK A., *Application of nanoparticles for magnetic hyperthermia for cancer treatment–the current state of knowledge*, Cancers, 2024, 16(6), DOI: 10.3390/cancers16061156.
[48] TARASEVYCH Y., SZCZECH M., *Comparative study of models and a new model of ferrofluid viscosity under magnetic fields and various temperatures*, Tribologia, 2024, 307(1):135–145, DOI: 10.5604/01.3001.0054.4666.
[49] WANG L.X., KONG X.Y., ZHOU T.J., *A computational study on effects of PID temperature target and RF frequency for PID-controlled nonablative RF cosmetic systems*, Lasers Surg Med, 2024, 56(10):865–879, DOI: 10.1002/lsm.23855.
[50] XING X., SONG C., *A novel electrode to achieve balance between anastomotic strength and tissue thermal damage for radiofrequency-induced intestinal anastomosis*, Acta Bioeng Biomech,, 2023, 25(3): 3–13, DOI: 10.5277/ABB-00278-2015-04.
[51] YAMAZAKI A., KAGAMI T., KUWAHATA A., YABUKAMI S., *Development of magnetic hyperthermia coil system for wide treatment temperature area on neck and breast cancer models*, IEEE Trans Magn, 2025, DOI: 10.1109/TMAG.2025.3551775.
[52] ZHANG C., SHI J., LI B., YU X., FENG X., YANG H., *Magnetic resonance imaging-guided radiofrequency ablation of breast cancer: a current state of the art review*, Diagn Interv. Radiol, 2024, 30(1):48–54, DOI: 10.4274/dir.2022.221429.